JOURNAL OF CATALYSIS **172,** 146–159 (1997)
ARTICLE NO. CA971842

Influence of Ceria on the Dispersion and Reduction/Oxidation Behaviour of Alumina-Supported Copper Catalysts

M. Fernández-García,*[,1] E. Gómez Rebollo,* A. Guerrero Ruiz,† J. C. Conesa,* and J. Soria*

*Instituto de Catálisis y Petroleoquímica, CSIC, Campus Universitario de Cantoblanco, 28049-Madrid, Spain; and †Dpto Química Inorgánica, UNED, 28040-Madrid, Spain

Received April 1, 1997; revised June 26, 1997; accepted June 30, 1997

A study using TEM combined with electron diffraction (ED), several spectroscopies (IR, ESR, XPS), and mass spectrometry-temperature programmed surface reaction of adsorbed NO is carried out on a $Cu/CeO_x/Al_2O_3$ catalyst and on similar specimens without Ce or Cu. TEM shows a preferential nucleation of the oxidized Cu phase on the ceria-rich regions, leading to a particle size in the Cu-containing phase smaller than that found in the Al_2O_3-supported system and decreasing the formation of the $CuAl_2O_4$ spinel. The Cu–Ce interaction developed in the calcination treatment also gives significant stability against sintering of the metallic copper phase formed during H_2 reduction. After reduction, the Ce-containing sample shows higher resistance to reoxidation of the surface copper phase by NO to the Cu^{2+} state (in comparison to Cu/Al_2O_3). On the basis of XPS-Ar^+ sputtering data, this may be related to partial coverage of the metallic Cu by reduced ceria in a way similar to that currently accepted for the SMSI effect; a capability of the Ce-containing support to stabilize the Cu^+ state may also contribute to this behaviour. This stable copper state appears in subsurface regions and is likely related to a new phase detected by TEM-ED and tentatively identified as a (Ce,Cu)–Al perovskite. The copper-cerium interaction affects also the reactivity of the catalyst towards NO, increasing (partly through a dissociative mechanism) the amount of adsorbed species which leads to low temperature NO and N_2/N_2O desorption, as well as shifting the decomposition temperatures of surface species containing N–N bonds (N_2/N_2O) formed upon NO adsorption. It is proposed that the addition of ceria may help to enhance the reductive elimination of NO by copper in automobile exhaust gases.

INTRODUCTION

The reductive elimination of NO has been extensively studied in recent years in connection with the control of exhaust emission (1). Due to the presence of noble metals (Pt, Rh, and Pd) in actual automobile emission control catalysts, these are expensive and alternative formulations are actively sought. In this search, copper-based systems have shown promising activity in catalyzing NO decomposition (2, 3) and NO reduction with CO (1, 3) or hydrocarbons in the presence or absence of oxygen (3). For the first two cases, several studies have evidenced that a redox-type mechanism involving a cupric-cuprous ion transformation is working under reaction conditions (4–6). The slow step of the reaction thus involves the interaction of one (in the NO + CO reaction) or two (in NO decomposition) NO molecule(s) with reduced copper centers. The reduction with hydrocarbons in absence of oxygen involves also the existence of reduced (metallic) copper centers (4). On the contrary, recent work has provided strong evidence that oxidized (Cu^{2+}) sites are the active centers for the NO reduction by hydrocarbons in oxidative conditions (7, 8). The slow step in this process has been proposed to correspond to an assisted (by NO_2-type species) abstraction of a hydrogen atom from the hydrocarbon (9).

Alumina-supported copper catalysts are among the most active (copper-based) ones in all the reductive NO reactions mentioned above (6, 8, 10). Inclusion of ceria in this system has been reported to be beneficial for the NO + CO reaction (10) and, due to its known oxygen storage function, this oxide may help to favor NO in its competition with oxygen for reaction with hydrocarbons. In addition, CuO_x/CeO_2 systems (stand alone or supported on alumina) display high activity for CO combustion (11). As shown in a recent review (10), metal-support interactions play an essential role in the catalytic behaviour of $Metal/CeO_x$ and $Metal/CeO_x/Al_2O_3$ systems. The presence of ceria is known to improve the dispersion of the active component via formation of M–O surface complexes in calcined samples (10); reductive atmospheres (hydrogen, hydrocarbons) at medium/high temperatures generally enhance metal-ceria interactions and, in some cases, induce SMSI-like behaviour (12). For Cu catalysts, these phenomena have not been investigated as thoroughly as for precious metals, and a basic knowledge of the interactions occurring among the catalyst components after calcination and/or activation treatments such as reduction will be required for the optimization of the catalytic properties of $Cu/CeO_x/Al_2O_3$ systems.

[1] Corresponding author. E-mail: ICPMF03@PINAR1.CSIC.ES.

0021-9517/97 $25.00

Keeping this goal in mind, a study of the basic interactions between Cu, CeO_x, and Al_2O_3 has been undertaken, using a multitechnique approach and examining the binary CeO_x/Al_2O_3 and Cu/Al_2O_3 systems in addition to the $Cu/CeO_x/Al_2O_3$ one. The interaction of the NO molecule with these systems is studied also, as it is well known that its activation by copper surface species is a key step in all the above mentioned catalytic processes.

EXPERIMENTAL METHODS

A Cu (4%)/CeO_2 (10%)/Al_2O_3 sample, here designated $Cu/CeO_x/Al_2O_3$, has been prepared by incipient wetness impregnation with an aqueous $Cu(NO_3)_2$ solution on a CeO_2/Al_2O_3 powder support. This binary support (with specific area $S_{BET} = 180$ m^2/g), designated CeO_x/Al_2O_3, was obtained previously by precipitation-deposition of ceria, adding slowly ammonia solution to an aqueous suspension of Al_2O_3 powder (γ-Al_2O_3, Condea, $S_{BET} = 200$ m^2/g) in a $Ce(NO_3)_3$ solution, followed by drying and calcination (4 h at 673 K, under flowing O_2/N_2 mixture). Previous work on this material (13) has shown that the preparation method used yields a higher ceria dispersion than the usual incipient wetness impregnation. The Cu-loaded catalyst, after being calcined in the same way, presents a specific BET surface area of 178 m^2/g. A similarly prepared Cu (4%)/Al_2O_3 reference catalyst, here designated Cu/Al_2O_3, has been also studied (BET area of 178 m^2/g).

X-ray Photoelectron and X-ray excited Auger spectra were obtained on pressed powdered samples with a Fisons Escalab 200R Spectrometer equipped with a pretreatment chamber, a Mg Kα anode (1253.6 eV) and a hemispherical electron analyzer, operating at a constant transmission energy pass (of 50 eV usually) and connected to a data station. The residual pressure in the analysis chamber was below 2.10^{-9} Torr. The spectra were recorded at room temperature, using low X-ray fluxes (60–120 W) to minimize X-ray induced reduction of Cu^{2+} and Ce^{4+} species. Under these conditions no catalyst reduction was observed. Survey scans (0–1100 eV binding energy) were recorded at an energy resolution of 3 eV. Regions of interest, i.e., $Cu_{2p_{3/2}}$, CuL_3VV, N_{1s}, Al_{2p}, $Ce_{3d_{5/2}}$, and C_{1s}, were taken at 0.1 eV resolution. Correction for static charge was made through reference to the C_{1s} peak at 284.9 eV. Where appropriate, the measured $Cu_{2p_{3/2}}$ photoelectron peaks were decomposed in contributions of different Cu valence states (approximated by Lorentzian/Gaussian shapes) and the areas of the resulting peaks (including satellite lines where present) used to determine the relative surface concentrations of the respective species (including in the calculations factors affecting quantitative data, viz. ionization cross section, electron escape depth, and instrumental sensitivity). Sputtering of the samples was carried out with an Ar^+ gun working at 1.5 keV and low ion currents (1 μA/cm^2). Previous experience indicates that under these conditions erosion of the solid surface proceeds at rates around 6–8 Å/min.

TEM experiments were carried out using a JEOL 2000FXII (0.31 nm point resolution) equipped with a LINK probe for EDS analysis. Microscopy samples were crushed in an agathe mortar and suspended in cyclohexane. After ultrasonic dispersion, a droplet was deposited on a nickel grid supporting a perforated carbon film. Several portions of the sample were examined at low magnifications performing simultaneous EDS analysis. Electron difractograms, micrographs, and, when necessary, dark field images were recorded for selected areas of the sample, with compositions previously characterized by EDS. Ring positions and lattice spacings in electron diffraction diagrams were refined by digitization of the diffraction images obtained and extraction of diffraction profiles via computer-controlled densitometry of the circular pattern. Simulation of electron diffraction profiles was carried out using the InsightII package made by Molecular Simulations, Inc.

FTIR spectra were recorded with a Nicolet 5ZDX Fourier Transform Spectrometer (4 cm^{-1} resolution, 100 scans). Powder samples were pressed into self-supporting wafers of ca 10 mg/cm^2 thickness and mounted in a Pyrex IR cell, assembled with greaseless stopcocks and NaCl windows, where catalysts could be treated under flowing gas at temperatures in the range 373–773 K. Pretreated samples were cooled to room temperature and the spectra recorded at beam temperature (estimated to be ca 320 K). The spectra of adsorbed species were extracted through subtraction of background and gas phase contributions and base line correction.

ESR spectra were obtained at 77 K with a Bruker ER200D system working in the X-band and calibrated with diphenyl-picryl-hydrazil ($g = 2.0036$). Quantitation of paramagnetic species was made by comparing doubly integrated intensities with those of a $CuSO_4 \cdot 5H_2O$ standard. Small quantities of sample (10–15 mg) were placed in a quartz probe cell equipped with greaseless stopcocks, where they were subjected to high vacuum, heating, and adsorption treatments.

Adsorption of CO and NO (Carburos Metálicos, of commercial purity, purified by freeze/pump/thaw methods before use) on the samples was performed at room temperature (for IR) or 77 K and above (for ESR) at a pressure of 10 Torr (1 Torr = 133.3 N $\cdot$ m^{-2}). Evolution of the samples after contact with NO was followed by ESR and IR for a period of 24 h. Temperature-programmed surface reaction (TPSR) experiments were carried out on samples (ca 30 mg) reduced at 723 K during 1 h, outgassed, and contacted with 10 Torr of NO during 1 h. MS-TPSR (mass spectrometry-temperature programmed surface reaction) spectra were taken during a temperature ramp of 5 K/min up to 723 K under vacuum using a mass spectrometer (Balzers QMG 125).

RESULTS

Results are presented here classified by the experimental technique used to obtained them. Assignment of several spectral features is also included in this section in aiming to facilitate a multitechnique approach to the discussion.

Preliminary characterization data. Both $Cu/CeO_x/Al_2O_3$ and Cu/Al_2O_3 samples (in the calcined state) failed to display in their XRD diffractograms peaks ascribable to Cu-containing phases; only broad features due to the CeO_2 and γ-Al_2O_3 phases with small crystallite sizes were discerned.

XPS data. XP spectra were taken on Cu/Al_2O_3 and $Cu/CeO_x/Al_2O_3$ samples after heating under vacuum or H_2 in the pretreatment chamber. In a first run, monitoring of the copper "visibility" during reduction (presumably affected by metal sintering) was the main aim. The XPS peaks corresponding to the Al_{2p}, $Ce_{3d_{5/2}}$, and $Cu_{2p_{3/2}}$ lines and the Cu Auger LMM peak were collected; binding energy, Cu Auger parameter (sum of XPS binding energy and Auger peak kinetic energy) and peak area ratios for the relevant steps of the treatment are given in Table 1. A first treatment in vacuum at 673 K led to a decrease in Cu/Al ratio for both samples, more markedly in sample Cu/Al_2O_3. This ratio was not appreciably modified upon subsequent reduction in H_2 at 423 K, but decreased further when the reduction temperature was increased up to 723 K, the effect being again considerably stronger for the Cu/Al_2O_3 sample. In principle, this decrease would indicate just sintering. The alternative possibility that such decrease in the Cu/Al ratio may be due to diffusion of Cu cations into the alumina support (to give a $CuAl_2O_4$-like structure) is unlikely as treatment in H_2 at 723 K is known to be enough to completely reduce Cu^{2+} from $CuAl_2O_4$ to metallic particles (14). Therefore, the much lower decrease in Cu/Al ratio observed in the $Cu/CeO_x/Al_2O_3$ sample respect to the Cu/Al_2O_3 specimen implies that sintering of the Cu particles is reduced by the presence of cerium.

TABLE 1

XPS Data (Run 1): $Cu_{2p_{3/2}}$ Binding Energy (eV), Cu LMM Auger Parameter α (eV) and XPS Cu/Al Intensity Ratio, Measured for the $Cu/CeO_x/Al_2O_3$ (CuCeAl) and Cu/Al_2O_3 (CuAl) Samples after Several Activation Treatments

Treatment (sequential)	CuCeAl			CuAl		
	$Cu_{2p_{3/2}}$ B.E.	α	I_{Cu}/I_{Al}	$Cu_{2p_{3/2}}$ B.E.	α	I_{Cu}/I_{Al}
Vac. RT	933.8	1848.9	1.44	934.5	1849.6	1.15
	935.2	1851.6				
Vac. 673 K	933.7	1849.8	1.28	932.9	1850.8	0.56
	935.5	1852.0		934.4	1849.3	
H_2 423 K	933.7	1849.0	1.30	933.0	1851.3	0.48
	935.5	1851.4		934.5	1849.9	
H_2 523 K	932.5	1851.2	0.63	932.4	1851.5	0.23
	935.3	—		934.6	—	
H_2 723 K	932.7	1851.3	0.45	932.4	1851.3	0.07

TABLE 2

XPS Data (Run 2): $Cu_{2p_{3/2}}$ and $Ce_{3d_{5/2}}$ Binding Energies (eV), Cu LMM Auger Parameter α (eV), Intensity of the Ce^{4+} Satellite at 914 eV (Expressed as Percentage of Total Ce Peaks Intensity) and Ce/Al, Cu/Al, and Cu/Ce Intensity Ratios Obtained during the Second XPS Run on the $Cu/CeO_x/Al_2O_3$ Sample (See Text for Details)

Pre-treatment	$Cu_{2p_{3/2}}$ B.E.	α	$Ce_{3d_{5/2}}$ B.E.	% Ce^{4+} satel.	I_{Ce}/I_{Al}	I_{Cu}/I_{Al}	I_{Cu}/I_{Ce}
Vac. RT	933.7 (68)	1848.5	883.0	10	10.3	1.59	0.15
	935.5 (32)	1851.4					
H_2 723 K	933.0	1850.9	882.8	9	10.9	0.67	0.061
Sputt. 1 min	933.1	1851.0	883.0	9	10.5	0.71	0.068
2 min	933.2	1850.9	883.1	9	10.6	0.84	0.079
3 min	933.4	1848.5	882.8	8	9.7	1.42	0.145
4 min	933.4	1848.7	883.1	7	9.3	1.44	0.155
5 min	933.6	1848.6	883.1	7	9.3	1.55	0.165
7 min	933.6	1848.7	883.0	7	11.0	1.46	0.135
10 min	933.5	1848.9	883.1	6	11.5	1.32	0.115
15 min	933.6	1848.8	883.1	4	11.7	1.25	0.105
20 min	933.6	1849.0	883.0	4	12.6	1.03	0.082
$+O_2$ 10^{-3} Torr	933.7	1848.6	883.2	4	—	—	—

Note. Values in parenthesis indicate percentage of the corresponding copper state.

In a second run, freshly calcined $Cu/CeO_x/Al_2O_3$ samples (this experiment was repeated twice) were subjected to heating in vacuo up to 473 K, then under H_2 (500 Torr) at 523 and 723 K and finally to sputtering with Ar^+ ions during 1- or 5-min intervals, cumulatively up to a total of 20 min. Intermediate evacuation of the chamber during reduction was made in order to minimize interferences by buildup of water vapour pressure. After the last part of each H_2 treatment, the sample was cooled in H_2 and outgassed at room temperature. Finally, a passivation by contacting with 10^{-3} Torr O_2 during 15 min was carried out. Data obtained in this second type of XPS run are given in Table 2. Similar reduction and sputtering experiments were performed on the ceria/alumina support, the results are given in Table 3.

A survey of literature data (Table 4; Refs. (15–19)) indicates that copper species (Cu^{2+}, Cu^+, and Cu^0) inserted in bulk phases can be differentiated by their characteristic binding energies in addition with their Auger parameters, α. However, when the copper phase is highly dispersed and in intimate contact with supports, as it occurs for Cu ions in zeolites or small Cu^0 particles supported on Al_2O_3 (Table 4), $Cu_{2p_{3/2}}$ energies and particularly Cu Auger parameters may deviate significantly from the corresponding bulk values. This can be ascribed to both initial state effects, i.e. variation of the core level energies with cluster size, and final state effects, i.e. different ease of electronic relaxation (in comparison to bulk oxides or metals) originated by the

TABLE 3

$Ce_{3d_{5/2}}$ Binding Energy (eV), Intensity of Ce^{4+} Satellite at 914 eV (Expressed as Percentage of Total Ce Intensity) and Ce/Al Intensity Ratio Obtained for the CeO_x/Al_2O_3 Sample during a XPS Run Similar to That Reported in Table 2 (See Text for Details)

Treatment	$Ce_{3d_{5/2}}$ B.E.	% Ce^{4+} satel.	I_{Ce}/I_{Al}
Vac. RT	882.9	11	34.2
H_2 723 K	883.0	10	36.1
Sput. 1 min	883.1	8	37.6
2 min	883.1	7	37.1
4 min	883.1	7	38.2
5 min	883.1	7	35.5
10 min	883.1	7	34.2
20 min	883.2	7	31.4
$+O_2$ 10^{-2} Torr	883.0	8	—

dominant effect of the electronic density distribution in the support.

The data in Table 4 highlight the difficulty in assigning XPS contributions when more than one copper valence state may be present and additionally highly dispersed forms coexist with bulk phases. Anyway, valence states have been tentatively ascribed to the Cu XPS peaks observed here so that overall trends can be identified. The initial $Cu/CeO_x/Al_2O_3$ calcined sample contains a mixture of a $CuAl_2O_4$-like surface phase and another phase with a XPS binding energy characteristic of a CuO-like component although the Auger parameter may suggest a Cu^+ compound. As seen in Table 1, both species are scarcely affected by outgassing at 673 K and reduction at 423 K. Higher reduction temperatures (523 K) yield a transformation of the latter phase to Cu^0, completed at 723 K with the reduction of the aluminate. For the Cu/Al_2O_3 sample, a reduced copper phase appears already after heating under vacuum.

TABLE 4

Representative Values of $Cu_{2p_{3/2}}$ Level Binding Energy (eV) and Cu LMM Auger Parameter (eV), Reported in the Literature for Copper Species in Several Well-Defined Materials

Cu species (sample)[a]	$Cu_{2p_{3/2}}$ B.E.	α	References
Cu_T^{2+} (Cu spinels)	935.5	1852.9	(15, 16)
Cu_O^{2+} (Cu spinels)	934.0	1851.4	(15, 16)
Cu^{2+} (bulk CuO)	933.8	1851.0	(17)
Cu_T^{+} (Cu spinels)	932.8	1848.6	(15, 16)
Cu_O^{+} (Cu spinels)	931.3	1849.6	(15, 16)
Cu^+ (bulk Cu_2O)	932.5	1849.6	(17)
Cu^{2+} ions (exchanged in zeolites)	935.2	1849.5	(18)
Cu^+ ions (exchanged in zeolites)	933.8	1847.2	(18)
Cu^0/Al_2O_3[b]	933.4	1849.0	(19)
Cu^0/Al_2O_3[c]	932.8	1851.6	(19)

[a] T, Tetrahedral sites; O, Octahedral sites.
[b] Cu small particles. Surface coverage 6×10^{13} atom cm^{-2}.
[c] 14 Å thick Cu layer.

Subsequent sputtering experiments lead to the observation in the $Cu/CeO_x/Al_2O_3$ sample of an oxidized state, particularly evidenced after 3 min of treatment. The observation of an oxidized state could be due either to a bombardement-induced solid state reaction (in the surface region), whereupon copper particles become oxidized, or to the elimination of the Cu^0 phase during sputtering, leaving exposed some oxidized species previously existing in a subsurface region. Although decomposition of the XPS peaks in the sputtered material is not reported in Table 2, it should be mentioned that a peak with binding energy above 935 eV was consistently observed throughout the series, suggesting that a minor part of the copper detected is in the rather stable state of the spinel phase; this agrees with the reappearance of the characteristic Cu^{2+} shake-up satellite. After 3 min of sputtering, however, most of the visible copper would be present mainly in the Cu^+ state, on the basis of the Auger parameter, although the permanence of some Cu^0 contribution cannot be ruled out.

The valence state of cerium can be ascertained qualitatively from the intensity of the satellite peak at ca 914 eV, characteristic of the Ce^{4+} state (it is absent in pure Ce_2O_3). In CeO_2, this peak bears to ca 14% of the total integrated intensity of the Ce_{3d} transitions (20). In both $Cu/CeO_x/Al_2O_3$ and CeO_x/Al_2O_3 samples the starting value is ca 10%, indicating the presence of some Ce^{3+}. A ratio value of 9.5% ± 1% has been indicated as typical of reasonably dispersed, highly loaded CeO_x/Al_2O_3 systems, which presumably contain a precursor of the $CeAlO_3$ perovskite (20). H_2 reduction leads to a moderate decrease in the Ce^{4+} peak; this decrease becomes larger during sputtering, the effect being substantially stronger in the $Cu/CeO_x/Al_2O_3$ sample than in the CeO_x/Al_2O_3 support. Thus the change from Cu^0 to Cu^+ observed in XPS during sputtering is accompanied by an enhancement in the Ce^{3+} content, which is much more marked than in the absence of copper. Depending on which of the two previously mentioned explanations for the observation of Cu^+ upon sputtering actually applies, this would suggest either that the surface reaction induced by Ar^+ bombardment implies a redox process of the type

$$Ce^{4+} + Cu^0 \rightarrow Ce^{3+} + Cu^+, \qquad [1]$$

or that the subsurface phase contains, together with copper, cerium in a predominantly Ce^{3+} state. The hypothesis based on process [1] agrees less well with the results after 7 min sputtering, where a strong decorrelation between the amount of both elements is found. The existence of a subsuperficial phase is then a more likely explanation for the overall results of the sputtering experiment. Note also that passivation scarcely changes the Ce satellite intensity, implying that the Ce^{3+} involved in this situation is much more stable than in the case of reduced pure ceria, as happens with $CeAlO_3$ or related structures (10).

The behaviour of the XPS peak intensities given in Tables 2 and 3 is also noteworthy. The overall Ce/Al intensity ratio in the CeO_x/Al_2O_3 support is substantially higher than in the $Cu/CeO_x/Al_2O_3$ sample; this implies that, in the latter, the surface ceria phase has been affected by the subsequent deposition of copper. This could correspond to preferential coverage of the ceria phase with copper (note that the overall atomic Cu/Ce ratio for the $Cu/CeO_x/Al_2O_3$ sample is ≈1.1) or to the formation of some specific compound between them. An alternative reasoning based on the increase of the ceria particle size is not in agreement with the XRD results that do not show significant differences between the calcined $Cu/CeO_x/Al_2O_3$ and CeO_x/Al_2O_3 samples.

Upon subsequent reduction of the catalysts, a decrease is observed in the Cu peaks (Table 1); the overall Ce intensity does not change much, as expected if it interacts strongly with alumina. Sputtering on the CeO_x/Al_2O_3 support (Table 3) yields a relatively steady value for the Ce/Al ratio during the first stages followed by a slow decrease. For the $Cu/CeO_x/Al_2O_3$ sample, in the first minutes the Cu line strongly grows, leading to increases in the Cu/Al and Cu/Ce ratios by factors of up to 2.3 and 2.75, respectively, while that of cerium decreases noticeably, the effect being somewhat reversed for longer sputtering times.

TEM data. The Cu/Al_2O_3 sample presents in the TEM micrographs a dominant ill-crystallized phase and a small fraction of larger crystals. The latter have sizes around 1 μm, and electron diffraction performed on them indicates symmetry and spacings corresponding to the spinel structure $CuAl_2O_4$ (data not shown). The less crystallized part presents an appearance similar to that of the parent γ-Al_2O_3 (not shown); EDS analysis on this part of the sample yielded Cu/Al ratios varying between 0.1 and 0.4. Electron diffraction patterns recorded on any of these areas give well-defined polycrystalline rings (not shown) clearly identifiable from their spacings as due to the $CuAl_2O_4$ phase. No electron diffraction rings ascribable to CuO or to any other Cu-related phase (except for the cited spinel) were detected.

The $Cu/CeO_x/Al_2O_3$ sample revealed a more complex structure. As for Cu/Al_2O_3, a small amount of large crystals (in this case with size around 0.1–0.2 μm) were detected and identified as $CuAl_2O_4$ (not shown). The main, less crystalline part has heterogeneous composition, according to the EDS analysis (Fig. 1). The higher Cu/Al ratios are obtained for those areas displaying the higher Ce/Al ratios, showing that Cu is distinctly associated with cerium in the catalyst.

Electron diffraction diagrams also yield different components in this material (Figs. 2A and 2B). The main Cu-related phase in Al-rich areas is $CuAl_2O_4$, while in Ce-rich ones is CuO; in both of them the only Ce-related phase clearly detectable is CeO_2. The morphology of the

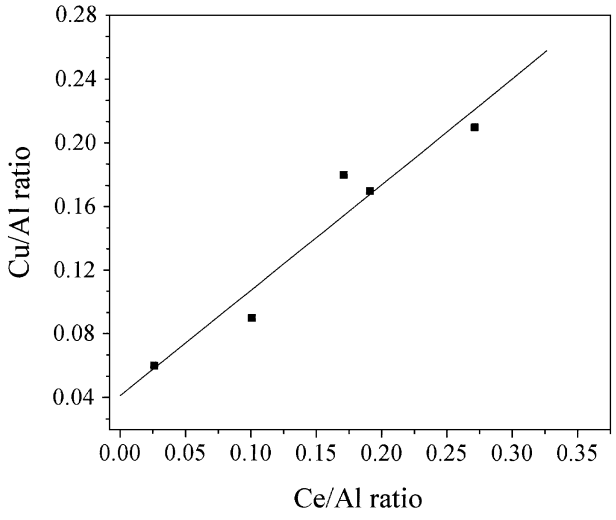

FIG. 1. EDS data from several locations of the $Cu/CeO_x/Al_2O_3$ catalyst. A linear fit (solid line) is included to highlight the correlation between the Cu and Ce components.

Cu-containing component also presents differences. In this case, dark field images were obtained to improve contrast. Representative images of that kind, obtained on areas with different Ce/Al ratios, are given in Figs. 3A and 3B. Particle size analysis of these images, counting more than 200 particles in each case, yields size distribution histograms (Fig. 4) which show in the Al-rich region a broader distribution, peaked at a higher particle size.

A similar examination was carried out on specimens subjected to H_2 reduction at 723 K followed by passivation before exposing to the atmosphere. On the Cu/Al_2O_3 sample, electron diffraction shows again $CuAl_2O_4$ as the only observable Cu-containing phase (data not shown). This indicates that exposure to atmosphere, even when carried out with a previous passivation step, completely reoxidizes any metallic copper particle and does not result in detectable CuO microcrystals (big CuO crystals with a weak interaction with alumina may, however, become a physically separate phase during the TEM sample preparation). For some regions of the images, the diffraction rings show now a more patchy appearance than in the initial calcined sample; this implies that larger crystals, and in a smaller number, have been formed, allowing us to distinguish partially the diffraction spots of individual crystallites. On the contrary, large crystals of ca 1 μm size, similar to those found in the calcined material, do not appear.

For the reduced $Cu/CeO_x/Al_2O_3$ sample, neither $CuAl_2O_4$ nor pure copper oxide or metal are revealed clearly in the electron diffraction patterns of the specimen (data not shown). Several diffraction exposures were taken in different regions of this sample and in some of them a weak but distinct ring was detected indicating a spacing of 1.54 Å (see Fig. 5). Another "nonassignable" ring, corresponding to a spacing around 1.19–1.18 Å, is contributing

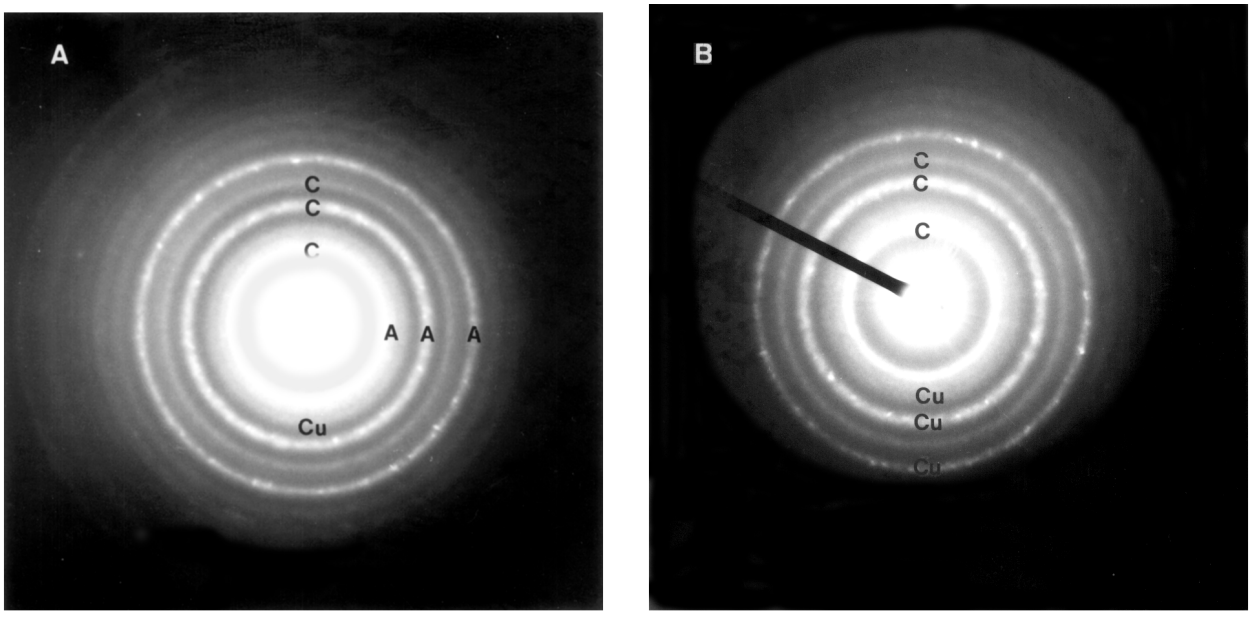

FIG. 2. Electron diffraction diagrams for two different zones of the $Cu/CeO_x/Al_2O_3$ catalyst: (A) Ce-rich zone; (B) Al-rich zone. Rings are assigned to: (C) ceria, (A) alumina, and (Cu)CuO (Fig. 2A) or $CuAl_2O_4$ (Fig. 2B) components.

to the outer side of the peak located at an average position of 1.21 Å, which also includes a ceria component at 1.24 Å (see Fig. 5). Additional small, discontinuous fragments of a ring located about 2.20 Å were observed in the image positives (more clearly in the negatives) but the densitometry averaging process leaves them out of Fig. 5. These rings were not detected in the same sample prior to reduction, nor in the Cu/Al_2O_3 material (reduced or not). This behaviour was observed in two independent samples (one of them used previously in XPS). Similar plane spacings only exist (among Ce, Al, and Cu compounds) in the $CeAlO_3$ perovskite (2.18, 1.54, and 1.20 Å (21)), although this phase has also a characteristic peak at $d = 3.77$ Å, which was not resolved. The possibility that such a phase could be present was, however, considered, taking into account that cation substitution and/or disorder could affect specifically the intensities of some diffraction lines. So, electron diffraction patterns were computed for pure $CeAlO_3$ and for the same phase with partial substitution of either Ce or Al by Cu, showing that substitution at the Ce position can lead to a substantial decrease of the $d = 3.77$ Å peak, while Al substitution does not. Thus the presence of a mixed (Ce,Cu)–Al perovskite is one sensible assignment for this new phase. Of course, we cannot discard the existence of another hitherto unknown phase. To our knowledge, no (Cu,Ce) mixed oxide structure has been reported in the literature. $CuLa_2O_4$ and $CuLaO_2$ structures are, however, known, but none of them has diffraction peaks agreeing with the observed features.

ESR data. ESR spectra taken for the Cu-containing materials show asymmetric signals in the $g > 2.00$ range, ascribable to paramagnetic Cu^{2+} ions (Fig. 6). In the initial calcined state and after outgassing at 673 K, spectra are dominated by an asymmetric, broad, and unresolved signal displaying extrema at positions $g \simeq 2.25$ and $g \simeq 2.04$. In addition, several shoulders can be detected in both cases, indicating the presence of another signal of nearly axial symmetry and more or less resolved four-component hyperfine splitting, its spin hamiltonian parameters lying close to $g_\perp = 2.06$, $A_\perp = 2.0 \times 10^{-3}\ cm^{-1}$ (the same for both samples), and $g_\parallel = 2.33$, $A_\parallel = 1.7 \times 10^{-2}\ cm^{-1}$ (for sample $Cu/CeO_x/Al_2O_3$) and $g_\parallel = 2.34$, $A_\parallel = 1.7 \times 10^{-2}\ cm^{-1}$ (for sample Cu/Al_2O_3). The latter signals indicate Cu^{2+} ions in a dispersed state, while the broad one will correspond to clusters or very small particles of an oxide phase with concentrated Cu^{2+} ions undergoing mutual magnetic coupling which will broaden the spectral lines. The total amount of unpaired spins in the calcined $Cu/CeO_x/Al_2O_3$ and Cu/Al_2O_3 samples corresponds respectively to 25 and 60% of the copper existing in them.

The intensity of the ESR signals decreases upon reduction in H_2 at $T = 723$ K (Fig. 6); after such treatment, only the well-resolved Cu^{2+} signal remains, but with reduced intensity. NO adsorption at 77 K does not change to a substantial extent the Cu^{2+} signal; a new ill-resolved line at $g \leq 2.00$ appears which can be ascribed to adsorbed NO radicals, so that the overall integrated intensity increases (Fig. 7). When the sample is warmed at room temperature, the NO signal disappears, more rapidly in the case of sample Cu/Al_2O_3; the Cu^{2+} signal then substantially increases for sample Cu/Al_2O_3 (Fig. 6). The different rate of ESR signal recovery upon NO adsorption after reduction is shown in Fig. 7.

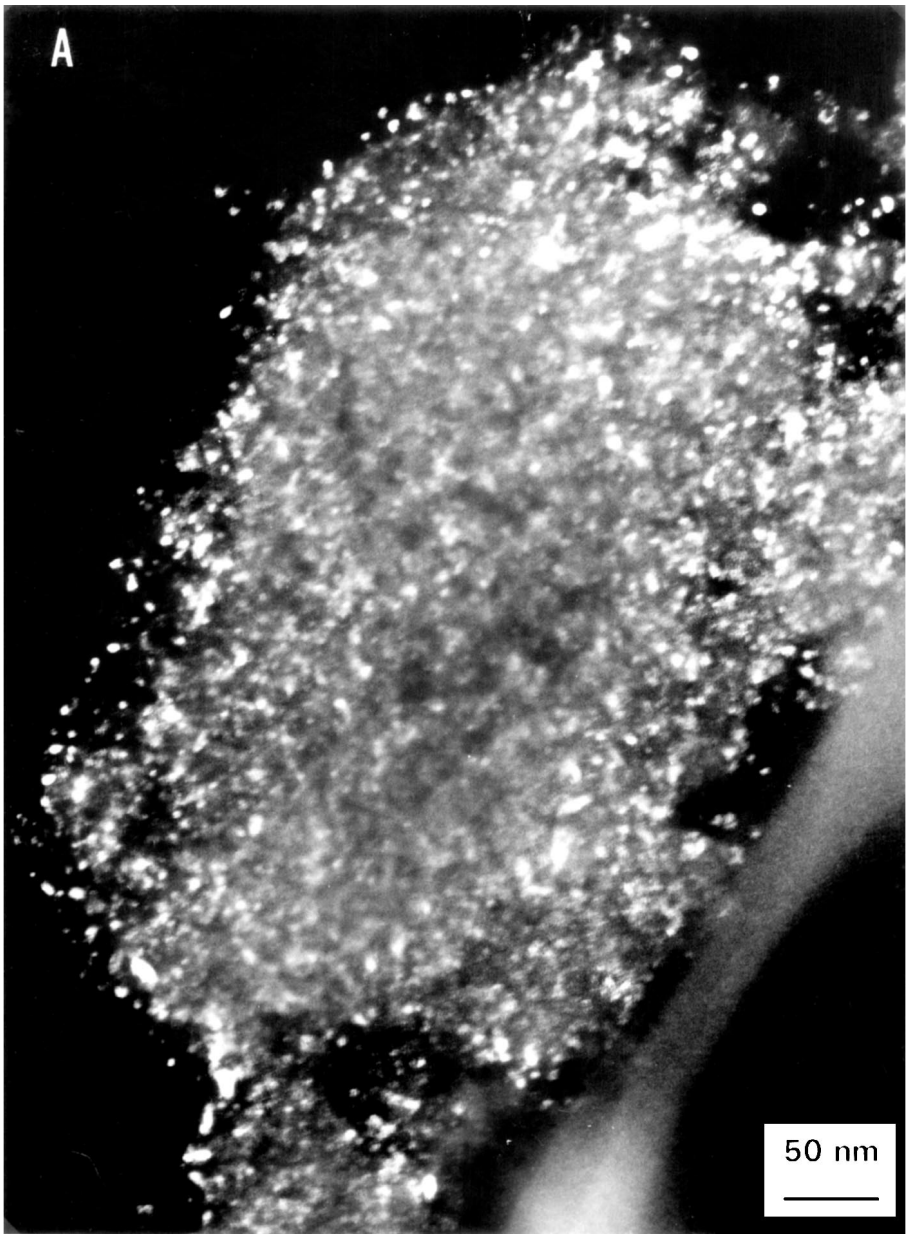

FIG. 3. Dark field TEM images corresponding to two zones of the $Cu/CeO_x/Al_2O_3$ catalyst: (A) Ce-rich zone; (B) Al-rich zone. Electron Diffraction diagrams for these two zones are shown in Figs. 2A and B, respectively.

For the Cu/Al_2O_3 sample, the increase in ESR intensity corresponds to the development of the well-resolved component. For the $Cu/CeO_x/Al_2O_3$ sample, the increase corresponds also to the development of the axial signal with resolved hyperfine structure, which parallel features appear at positions somewhat different from those of the Cu/Al_2O_3 sample, although certainly more similar to these latter than to those observed previously for the CuO_x/CeO_2 system (22). The best computer simulations of these signals were obtained with parameters $g_\parallel = 2.344$, $g_\perp = 2.062$, $A_\parallel = 1.70 \times 10^{-2}$ cm^{-1}, $A_\perp = 2.1 \times 10^{-3}$ cm^{-1}, $Q = 7.5 \times 10^{-4}$ cm^{-1} for sample Cu/Al_2O_3; $g_\parallel = 2.324$, $g_\perp = 2.059$, $A_\parallel = 1.66 \times 10^{-2}$ cm^{-1}, $A_\perp = 2.0 \times 10^{-3}$ cm^{-1}, $Q = 7.0 \times 10^{-4}$ cm^{-1} for sample $Cu/CeO_x/Al_2O_3$ (inclusion of the quadrupole interaction was necessary to reproduce correctly all peaks in the high field part of the spectrum). These values can be compared with those reported for CuO_x/CeO_2 samples (22): $g_\parallel = 2.265$, $g_\perp = 2.040$, $A_\parallel = 1.60 \times 10^{-2}$ cm^{-1}, $A_\perp = 1.3 \times 10^{-3}$ cm^{-1}.

IR data with CO and NO probe molecules. IR spectra were taken on both Cu/Al_2O_3 and $Cu/CeO_x/Al_2O_3$ samples, after reduction under 500 Torr H_2 at 723 K, outgassing at 523 K and addition of CO (10 Torr) at room temperature.

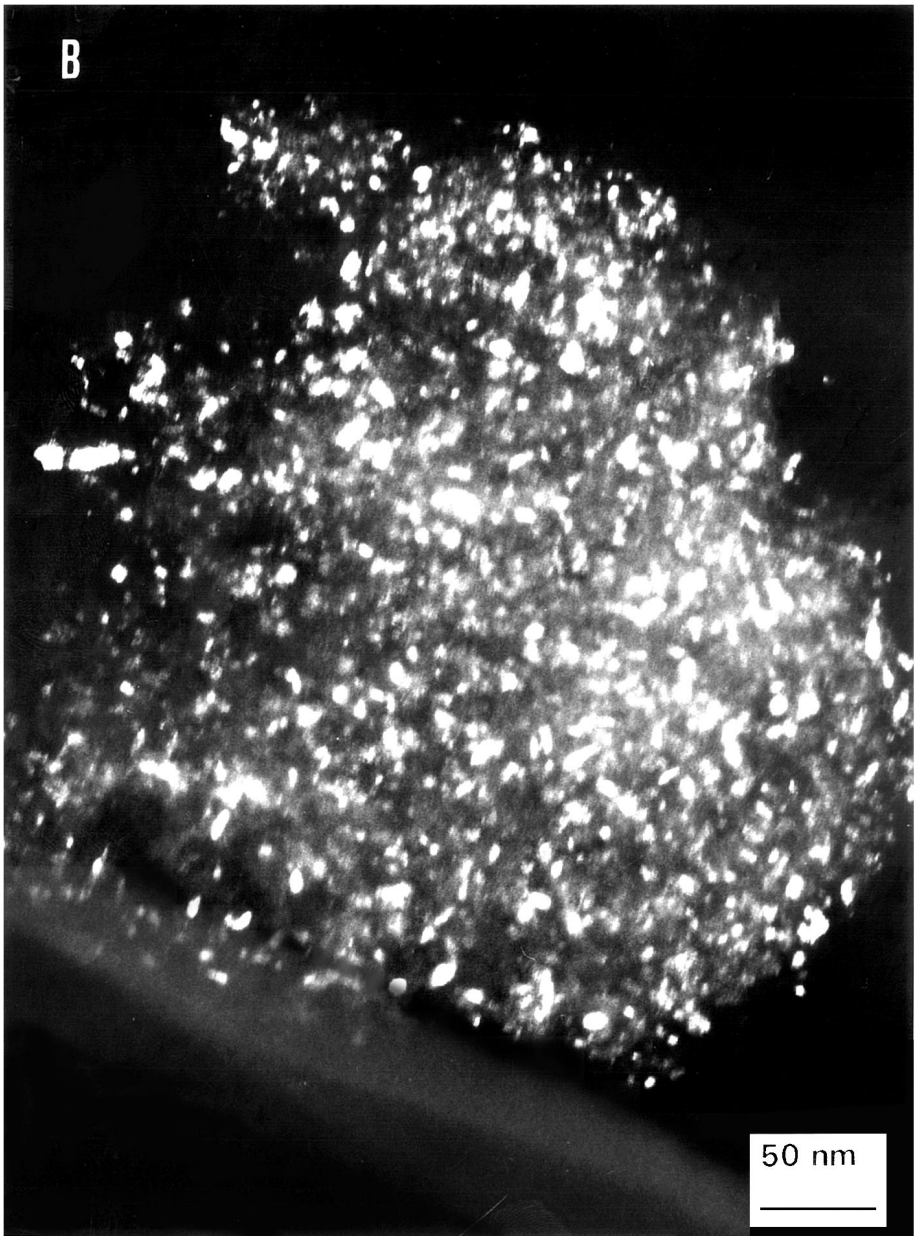

FIG. 3—*Continued*

The spectra obtained in the carbonyl bond region are given in Fig. 8. The $Cu/CeO_x/Al_2O_3$ sample presents one main peak located at 2115 cm^{-1}, accompanied by a much smaller one at ca 2000 cm^{-1}, while sample Cu/Al_2O_3 shows a doublet around 2100 cm^{-1}, with one component corresponding to a frequency of ca 2115 cm^{-1} and the sharper one located at 2100 cm^{-1}. For this latter sample a tail extending around 2050 cm^{-1} is observed, this suggests some broad contribution in that range. Another peak appears at higher wavenumbers (around 2185 cm^{-1}).

IR data were obtained also after NO adsorption on samples reduced in the same way. Apart from several bands in the range 1250–1700 cm^{-1} (data not shown), ascribable to nitrates, nitrites, and hyponitrites and which is too complex and ill-defined to be analyzed with confidence, several resolved peaks appear in the region above 1700 cm^{-1} (Fig. 9). For the Cu/Al_2O_3 sample, two main bands quickly develop, located at 2135 and 1884 cm^{-1}, with a smaller peak also appearing at 1920 cm^{-1} (Fig. 9E). The first peak can be ascribed to NO_2 adsorbed on Cu ions, while that at 1884 cm^{-1} is due to NO adsorbed on Cu^{2+} (23, 24) and is thus indicative of full copper oxidation. For the $Cu/CeO_x/Al_2O_3$ sample (Figs. 9A–C), a peak at 1800 cm^{-1}, assigned to NO adsorbed on Cu^+ (23, 24), appears together with peaks similar

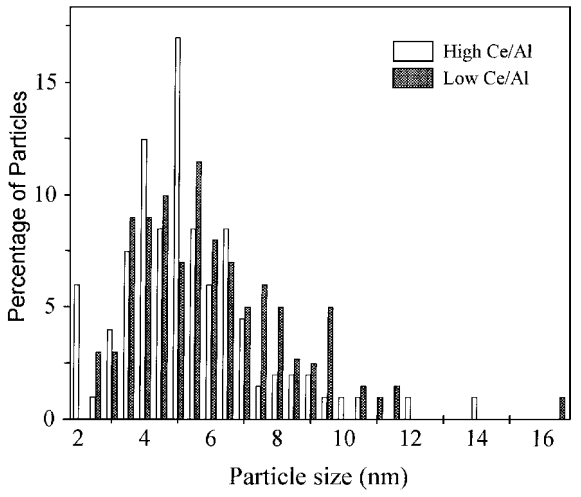

FIG. 4. Particle size histograms (from dark field TEM images) for the two zones of the $Cu/CeO_x/Al_2O_3$ catalyst shown in Figs. 3A and 3B.

to those observed in the Cu/Al_2O_3 sample. The intensity of this last group of peaks grows very slowly, as evidenced the comparison with the reduced Cu/Al_2O_3 catalyst behaviour (Fig. 9).

NO TPSR data. After NO adsorption on the 723 K reduced/outgassed samples, the evolution of the main desorption products (N_2, NO, and N_2O; NO_2 and O_2 were not obtained in significant amounts) during TPSR runs is displayed in Fig. 10. M/z values of 28 and 44 are ascribed to N_2 and N_2O only; after the previous reduction and outgassing a $T = 723$ K it is unlikely that the samples can keep

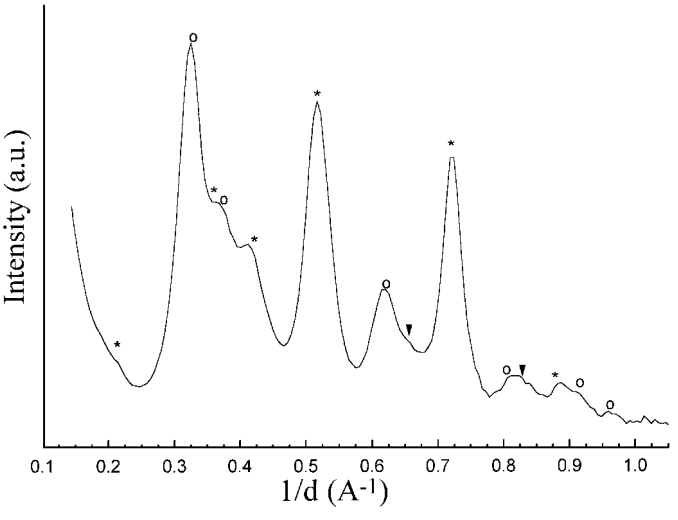

FIG. 5. Radial (angle-averaged) densitometry pattern of the electron diffraction rings observed in a Ce-rich zone of the reduced $Cu/CeO_x/Al_2O_3$ catalyst. Symbols indicate peaks expected for ceria (○) and alumina (∗); arrows mark features ascribable to other phase(s), possibly a (Cu,Ce)−Al perovskite. The abscissa axis is scaled to represent the inverse of the interplanar spacing distance ($Å^{-1}$).

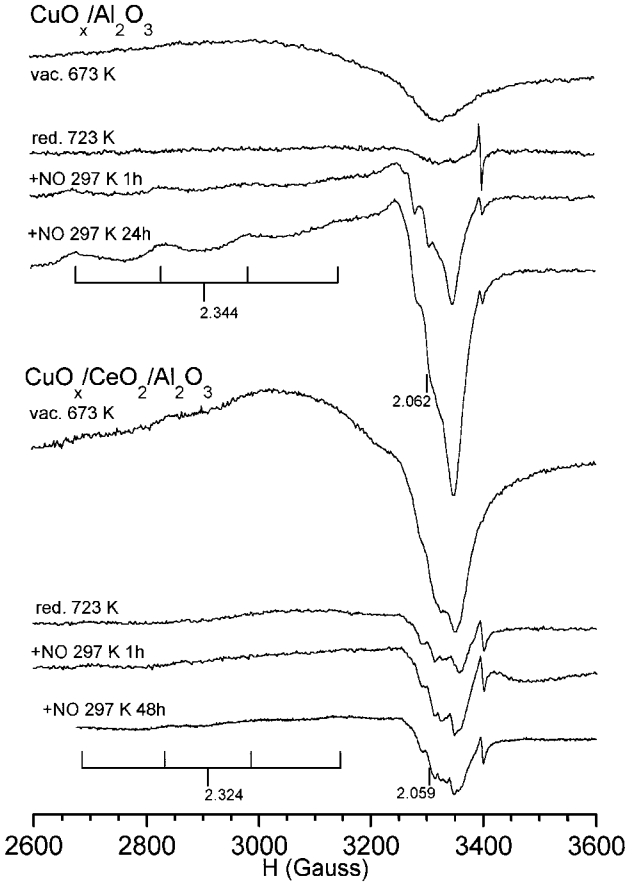

FIG. 6. ESR spectra of Cu/Al_2O_3 and $Cu/CeO_x/Al_2O_3$ samples after evacuation at 673 K, H_2 reduction at 723 K and contact with 10 Torr NO at different exposure times.

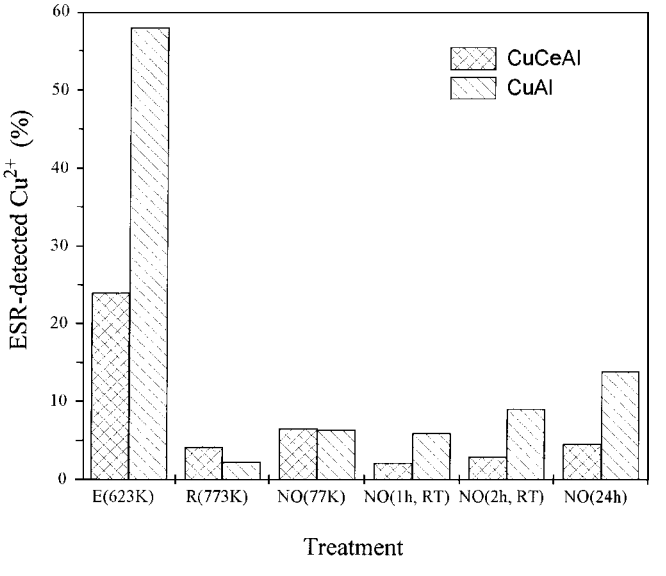

FIG. 7. Percentage of Cu^{2+} detected by ESR in samples $Cu/CeO_x/Al_2O_3$ (CuCeAl) and Cu/Al_2O_3 (CuAl) after evacuation at 623 K, reduction at 723 K, and contact with 10 Torr NO, first at 77 K and subsequently at room temperature during different periods.

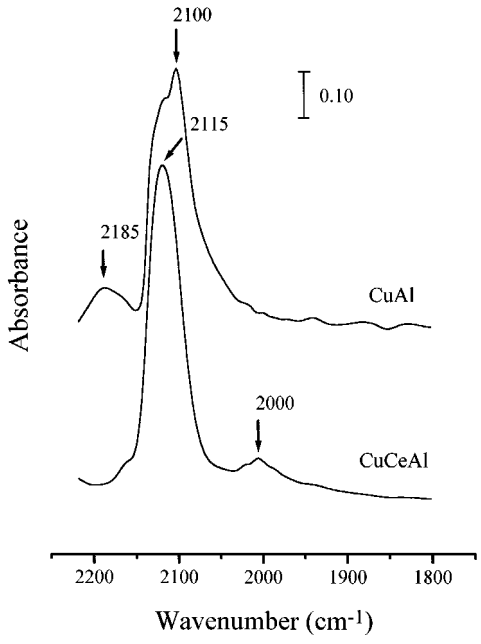

FIG. 8. FTIR spectra after adsorption of 10 Torr of CO on $Cu/CeO_x/Al_2O_3$ (CuCeAl) and Cu/Al_2O_3 (CuAl) catalysts reduced in H_2 at 723 K.

species able to desorb as CO or CO_2 in the temperature range used here. This was further checked by following secondary masses.

Desorption features are seen to concentrate in two temperature regions: one from near 320 K to ca 520 K, and the other one peaking at $T = 540$ K or above. The first one produces mainly NO and N_2 (with some N_2O appearing also for the $Cu/CeO_x/Al_2O_3$ sample), the second one, N_2 and N_2O. In the lower temperature range, NO desorption is seen to appear from all samples except alumina (which shows only a small amount of it around 570 K), while N_2 is produced only in the Cu-containing catalysts. On the other hand, the main N_2O desorption peak is seen to begin at rather different temperatures in these samples. The lowest desorption temperature occurs for the ceria/alumina support (onset around 450 K), while the $Cu/CeO_x/Al_2O_3$ sample only begins to desorb at ca 540 K; the Cu/Al_2O_3 sample has an intermediate behaviour. In this higher temperature range, the $M/z = 28$ mass peak presents a similar evolution as N_2O; since N_2 can conceivably result from decomposition of N_2O on the catalyst surface (not on the mass spectrometer chamber; the principal dissociation product of ionized N_2O is NO (25), which was not observed), the N_2 in this profile can be considered as a secondary product after N_2O generation.

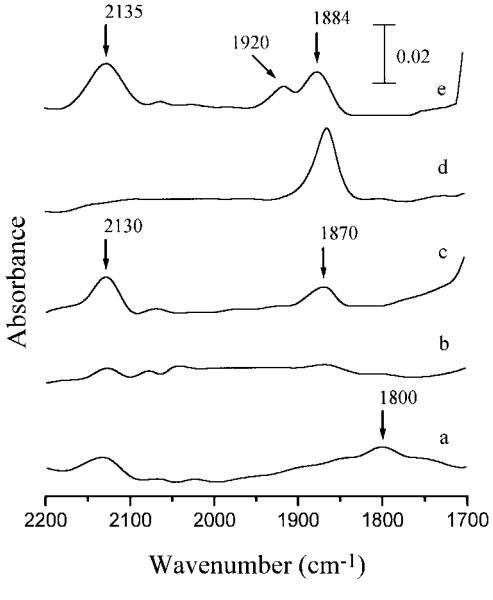

FIG. 9. FTIR spectra after the adsorption of 10 Torr of NO on Cu-containing catalysts: $Cu/CeO_x/Al_2O_3$ (CuCeAl) reduced in H_2 at 723 K (a, 5 min; b, 1 h; c, 3 h), calcined $Cu/CeO_x/Al_2O_3$ (d, 5 min) and Cu/Al_2O_3 (CuAl) reduced at 723 K (e, 5 min).

DISCUSSION

Structural Characteristics of the Materials Examined

The experimental data obtained provide several indications of Cu–Ce interactions. In discussing these, it is convenient to recall that previous work (13) indicated that this type of ceria-alumina support contains cerium both as small CeO_2 particles (partly detectable by X-ray or electron diffraction) and as bidimensional ceria patches, the reactivity of which is noticeably different from that of CeO_2. The support used here has a Ce content close to that giving the maximum amount of bidimensional patches. Obviously, the deposition of copper on a support where the surface exposes such a combination of cerium-related phases as well as Ce-free alumina can lead to the generation of several species that will complicate the interpretation of the results.

The Cu–Ce interactions are present already in the preparation of the calcined $Cu/CeO_x/Al_2O_3$ catalyst, as evidenced by the TEM-EDS data: copper concentrates in the areas with higher surface Ce contents, and furthermore, the Cu-related crystallite particles found on those areas have a noticeably smaller size than those found in the Ce-poor areas. This indicates an enhanced nucleation of the copper phase on the surface CeO_x patches during impregnation. It is noted also that the Cu-containing phase detected in the Ce-rich areas of $Cu/CeO_x/Al_2O_3$ is CuO rather than $CuAl_2O_4$; this means that the Ce-covered alumina surface is more inert than the bare one. The results show also that the fraction of Cu detectable by ESR as Cu^{2+} is lower in $Cu/CeO_x/Al_2O_3$ than in Cu/Al_2O_3, already in the calcined state. That fraction is even lower in CuO_x/CeO_2 systems (22). Although the reason for this is in principle not determined, these observations indicate that a significant part of the copper in the $Cu/CeO_x/Al_2O_3$ sample may be in a situation close to that existing in the CuO_x/CeO_2 system, even though the CeO_x/Al_2O_3 support seems to contain cerium

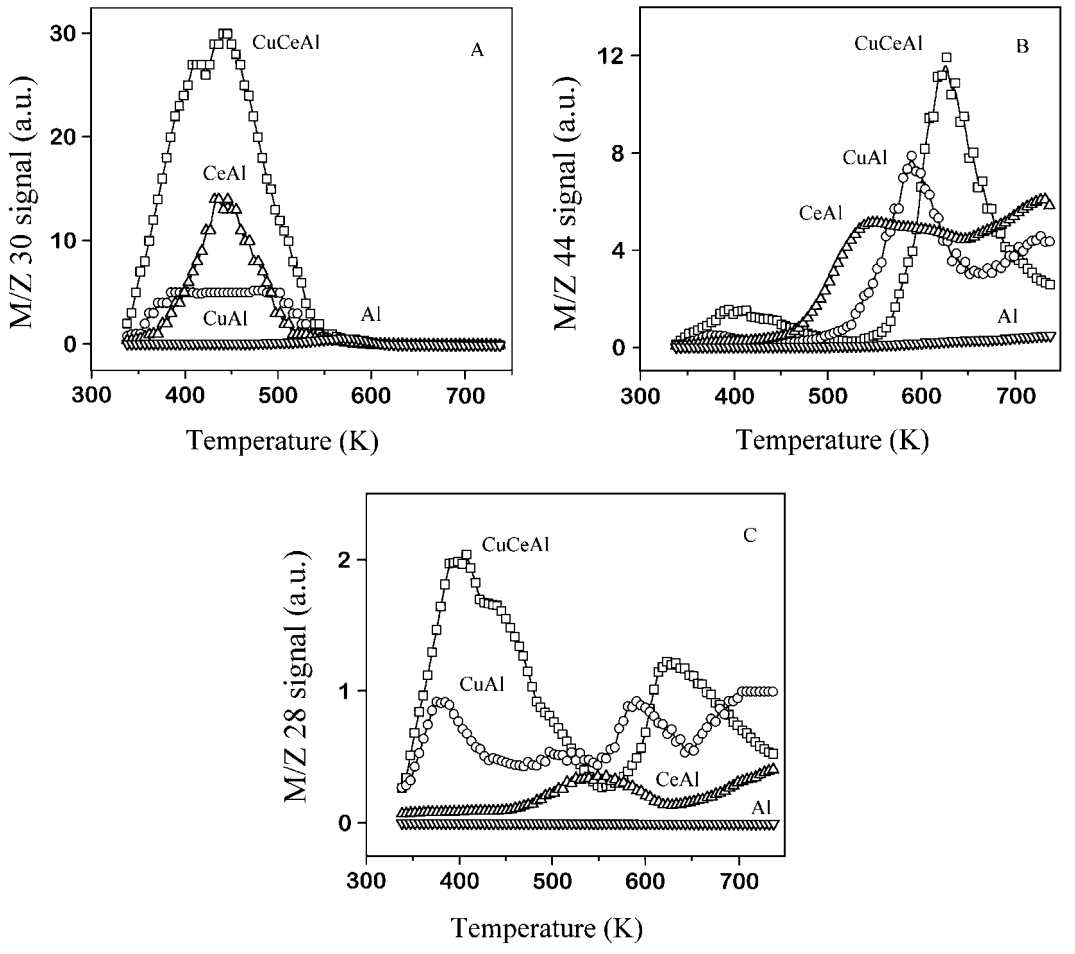

FIG. 10. MS-TPSR spectra obtained after NO adsorption on Cu/Al_2O_3 (CuAl) and $Cu/CeO_x/Al_2O_3$ (CuCeAl) catalysts and CeO_x/Al_2O_3 (CeAl) and Al_2O_3 (Al) supports previously reduced in H_2 at 723 K: (A) M/Z = 30 signal; (B) M/Z = 44 signal; (C) M/Z = 28 signal.

mostly as bidimensional patches. As to the highly dispersed Cu^{2+} giving well-resolved ESR lines, the similar parameters observed in both Cu/Al_2O_3 and $Cu/CeO_x/Al_2O_3$ samples indicate that they are both located in the free alumina surface.

The difference in size observed in Fig. 4 for the Cu-containing particles between the initial Cu/Al_2O_3 and $Cu/CeO_x/Al_2O_3$ samples is reproduced in the reduced catalyst. This is evidenced by the stronger fall in Cu XPS signal observed upon H_2 reduction in the Ce-free catalyst, indicating that the presence of cerium retards the sintering of the Cu particles and suggesting again a specific cerium–copper interaction. A difference is observed also in the surface of the reduced Cu-containing particles. Relatively high frequencies like those of the single main peak observed here (around 2115 cm^{-1}) are at the borderline between the frequency ranges normally ascribed to Cu^+ and Cu^0 adsorption sites (26, 27). Although XPS indicates the existence of essentially metallic Cu^0 after reduction, the 2115 cm^{-1} band may originate by adsorption on surface Cu atoms which have some positive charge ($\leq +1$) due to the presence of ceria entities at the metallic particle surface. In fact, the $Cu/CeO_x/Al_2O_3$ sample also presents an IR peak at 2000 cm^{-1} that is not easily ascribable to a CO or CO-related (carbonate, CO_2) species adsorbed on any Cu state; such band is commonly assigned in the literature to carbonyls absorbed on metal–support interface sites in metallic systems supported on reducible oxides (28). The peak at 2185 cm^{-1}, observed only for the Cu/Al_2O_3 sample, may be ascribed to CO adsorbed on less reducible Cu^{n+} ions located in the spinel phase.

A second indication of the existence of a Cu–Ce interface with catalytic implications is provided by the XP spectra obtained upon sputtering of the reduced $Cu/CeO_x/Al_2O_3$ sample. On supported catalysts, this latter operation normally leads to a gradual decrease of surface-dispersed phases. On the contrary, here it produces an initial increase in the Cu/Al ratio simultaneously to a small decrease in the Ce/Al ratio; this is followed by a turning point around 7 min of treatment, after which the Cu/Al ratio decreases, while the Ce signal intensity recovers. The behaviour in the initial stage (first 3 min of sputtering) is akin to that observed for systems presenting the SMSI (strong metal–support interaction)

effect, well documented for metals supported on reducible oxides such as TiO_2 (28) and generally accepted to result from the coverage of the surface of the metal by reduced (MO_x) species. Such covering of the metal, independently of the exact mechanism of generation, has been reported to occur in CeO_x-based systems containing precious metals (10, 12), although in some of these cases the coverage of the metallic phase was observed only at higher temperatures (>873 K) (10, 29).

It seems thus that in the supported Cu–Ce system examined here, the above-mentioned effect can develop to a significant extent at lower temperatures. However, a decoration-like phenomenon of the metallic particles alone does not account for the experimental results, since the maximum "uncovering" effect is observed well after 3 min of sputtering (about 5), roughly corresponding to the removal of a layer several tens of Å thick. This implies a substantial surface reconstruction from the state which presumably exists initially and points to a solid state reaction rather than to surface diffusion. A possible process could be, e.g. a reaction of the copper-containing phase with the ceria support during intermediate stages of the reduction process, giving a mixed oxidized phase, the outermost layers of which decompose back upon further reduction to give copper metal particles accompanied by, and possibly partially buried with, substantial amounts of ceria. Note, however, that a CeO_x layer covering copper-containing particles could not be discerned in any of the TEM images (obtained after passivation and exposure to air). After eroding away the outer layer, containing Cu metal and Ce, a subsurface region richer in Cu, where the dominant redox states are Cu^+ and Ce^{3+}, would then be observed.

The possible formation of a new phase in the $Cu/CeO_x/Al_2O_3$ sample upon H_2 reduction (followed by reoxidation at room temperature) as suggested by TEM-ED is therefore of interest. There is no certainty as to its nature, but its appearance only when Ce is present and the existence of a Ce^{3+} state stable under oxygen (detected by XPS after sputtering) agrees with the above given assignment to a (Ce,Cu)–Al perovskite. The redox state of Cu in that material is not known, but taking into account the relevant ionic radii (ca 0.67, 0.87, 1.15, 1.28, and 1.11 Å for Al^{3+}_{oct}, Cu^{2+}, Cu^+, $Ce^{3+}_{8\text{-coord}}$, and $Ce^{4+}_{8\text{-coord}}$, respectively), the hints that substitution might take place at the Ce site point to the Cu^+ state, which in turn, is correlated with the appearance of Ce^{3+} in the sputtering experiment. In sum, the TEM and XPS data, together are best explained assuming the existence of a mixed perovskite involving Ce^{3+} and Cu^+. Note that cation substitution in the (Ce,Cu)–Al phase needs some charge compensation; this may be achieved via oxidation of part of the remaining Ce^{3+} ions to Ce^{4+} or by the presence of oxygen vacancies, so that the material would have to be formulated as $Ce_{1-y}Cu_yAlO_{3-y}$ (assuming that no other defects appear). Since the amount of Ce^{3+} is not lower in reduced $Cu/CeO_x/Al_2O_3$ than in reduced CeO_x/Al_2O_3 the first alternative seems unlikely.

Effects of Cu–Ceria Interactions on Surface Reactivity

Further indications on the effect of ceria in the reactivity of surface copper entities are given by the spectroscopic data obtained upon NO adsorption. IR spectra show that adsorption centers able to form Cu^{2+}—NO surface complexes (characterized by a peak near 1885 cm^{-1}) appear in the Cu/Al_2O_3 sample already a few minutes after contact with NO, while on $Cu/CeO_x/Al_2O_3$ the same peak takes several hours to develop to a comparable extent. A similar effect is observed with ESR; the growth of the Cu^{2+} signals after NO adsorption is substantially faster for the Cu/Al_2O_3 sample than for $Cu/CeO_x/Al_2O_3$. Finally, the fact that after exposure to air the new phase detected by the electron diffraction phase might contain Cu^+ rather than Cu^{2+}, in contrast to the behaviour of Cu/Al_2O_3 (where $CuAl_2O_4$ is observed), would agree also with a slower reoxidation of the copper metal particles due, e.g. to partial coverage by ceria-derived entities. Since the $CeAlO_3$ perovskite is stable to oxidation under oxygen up to 873 K (10), the slowness of the full oxidation of copper to the Cu^{2+} state could also be related to a higher stability against oxidation of the mentioned (Ce,Cu)–Al phase. In any case, the data indicate that reoxidation of copper does not progress easily beyond the Cu^+ state when ceria is present and an intimate Cu–Ce contact is reached in the catalyst preparation stage.

An indication of mutual Ce and Cu influence is derived also from the NO TPSR profiles (Fig. 10). In principle, the low temperature evolution observed may come from adsorbed NO or from nitrite species (through decomposition). The former are adsorbed mainly on copper sites, as shown by the IR data of Fig. 9; such species have been reported to desorb around 390 K (24), and therefore may explain the 400 K peak. Nitrites may be adsorbed on both oxidized copper and the supporting oxide; the coincidence in NO desorption temperature between the CeO_x/Al_2O_3 support and the 450 K peak indicates that the latter has its main contribution coming from the ceria component, although some contribution from CuO_x may be present also, as the Cu/Al_2O_3 sample evolves NO in this temperature range. Note that the overall amount in the $Cu/CeO_x/Al_2O_3$ sample is higher that the sum of those observed for CeO_x/Al_2O_3 and Cu/Al_2O_3; the increase seems to affect to both the 400 and 450 K contributions, implying that the simultaneous presence of ceria and copper components enhances the NO adsorption capacity of both of them. This may be ascribed to the higher dispersion of the active phase reached in the $Cu/CeO_x/Al_2O_3$ sample; however, the IR data in Fig. 9 indicate that adsorbed NO species are formed in lower amounts on $Cu/CeO_x/Al_2O_3$. An explanation for this may be based on a dissociative pathway contribution; "weakly" adsorbed N atoms, that would remain undetected by IR, could lead

to NO evolution by recombining with oxygen-containing species. This enhanced NO adsorption, which does not result in Cu^{2+} nor in molecularly adsorbed NO, supports the hypothesis of a copper–ceria chemical interaction, possibly favouring the formation of some mixed phase, rather than simple geometrical blocking by coverage of the metal.

Low temperature (below 500 K) N_2 desorption appears only on Cu-containing samples and has the main peak at 380–400 K. Adsorbed N atoms, which demands previous NO dissociative adsorption on Cu metal particles (30), are probably in the origin of this feature. The higher intensity of this peak in sample $Cu/CeO_x/Al_2O_3$ further supports the hypothesis of an enhanced dissociative NO adsorption pathway. N_2O desorption in this temperature range resembles closely the N_2 one and would be then explained as result of recombination between N atoms and NO-containing molecules. The additional N_2/N_2O peak at ca 450 K observed for $Cu/CeO_x/Al_2O_3$ would result from a NO-containing species adsorbed on ceria. The N_2O (plus N_2) appearing at higher temperatures must result from more strongly held surface species, which seem to contain already well formed N–N bonds since NO does not appear at the same time. This part of the spectra shows, again, the important differences observed between the $Cu/CeO_x/Al_2O_3$ system and its "parent" Cu/Al_2O_3 and CeO_x/Al_2O_3 ones.

The main enhancing effect of the Cu–Ce interaction here refers to the low temperature processes leading to N_2O and N_2 formation. These molecules are products of the dissociation of the NO bond, and therefore, their amounts give a measure of the ability of the catalyst to break this bond. This is a relevant observation since the NO bond breaking is probably the slow step in reactions such as $CO + NO$ (6) or the $CO + NO + O_2$ (31). The efficiency in this dissociative process is certainly related with the copper oxidation state (6, 31), a property which in turn has been here demonstrated to be related with the Cu–Ce interaction. The increased NO (dissociative) adsorption capability, together with the higher surface mobility of N atoms observed in the reduced $Cu/CeO_x/Al_2O_3$ sample could be of beneficial influence for NO reduction processes. Particularly, a higher NO reservoir capability may help NO in its competition with O_2 in the $NO + CO + O_2$ reaction or in its selective reduction with hydrocarbons in SCR reactions.

CONCLUSIONS

The studies carried out reveal several aspects of interactions between copper and ceria in the $CuO_x/CeO_x/Al_2O_3$ system, which affect the structural and chemical characteristics of its components. Copper (in an oxidized phase) is deposited preferentially on the ceria component when the latter is present on the alumina carrier. This produces smaller amounts of the $CuAl_2O_4$ spinel that similarly loaded Cu/Al_2O_3 systems and decreased the amount of copper ions detected by ESR. As the IR/XPS results show, the resulting interaction leads to higher dispersion and resistance to sintering and, possibly, also to partial coverage by reduced ceria species of the metallic copper particles formed upon H_2 reduction. In that situation, copper is more resistant to oxidation into the Cu^{2+} state upon interaction with NO.

After reoxidation of the H_2-reduced sample, a new phase appears in the $Cu/CeO_x/Al_2O_3$ material, which might correspond to a $Ce_{1-y}Cu_yAlO_{3-y}$ surface perovskite stabilizing the Cu^+ and Ce^{3+} states; its formation would be easier than that of $CeAlO_3$ in the copper-free sample. The Cu–Ce interaction gives also a higher NO adsorption capability for the reduced $Cu/CeO_x/Al_2O_3$ catalyst with respect to the Cu/Al_2O_3 one. This affects mainly dissociative desorption which leads to low temperature N_2 formation; other surface species, which contain N–N bonds, require higher temperatures to desorb into N_2O and N_2, a fact which could be due to the more difficult oxidation of the mentioned mixed phase.

Overall, the data show a specific tendency of deposited copper to associate with surface ceria and become stabilized into the Cu^+ state. The observed changes in surface reactivity and reduction/oxidation behaviour might be significant for achieving a more efficient reductive activation of NO, which is the main path for reduction of NO by CO or the $NO + CO + O_2$ reaction in these systems. The higher NO adsorption capability may also be of significance for other NO abatement pathways in oxidative atmospheres.

ACKNOWLEDGMENTS

Financial help from CICYT (project 94-9835-CO3-O2) is acknowledged. Thanks are given to Dr. A. Martínez-Arias for fruitful discussions, to Mr. F. Sánchez Constenla for recording ESR spectra, and to Professor J. L. G. Fierro and Mr. E. Pardo for obtaining the XPS data. E.G.R. thanks the CICYT for a Ph.D. fellowship. M.F.-G. acknowledges also the CSIC for a postdoctoral contract under which part of this project has been carried out.

REFERENCES

1. Amiridis, M. D., Zhang, T., and Farrauto, R. J., *Appl. Catal. B: Environmental* **10**, 203 (1996).
2. Iwamoto, M., and Hamada, H., *Catal. Today* **10**, 57 (1991).
3. (a) Shelef, M., *Chem. Rev.* **95**, 209 (1995); (b) Iwamoto, M., Yahiro, H., Shundo, Y., Yu-u, Y., and Mizuno, N., *Shokubai* **32**, 430 (1990).
4. Shannon, I. J., Rey, F., Sankar, G., Thomas, J. M., Maschmeyer, T., Waller, A. M., Palomares, A. E., Corma, A., Dent, A., and Greaves, G. N., *J. Chem. Soc. Faraday Trans.* **92**, 4331 (1996).
5. Liu, D. J., and Robota, H. J., *Catal. Lett.* **21**, 291 (1993).
6. Fernández-García, M., Márquez-Alvarez, C., Rodríguez-Ramos, I., Guerrero-Ruiz, A., and Haller, G. L., *J. Phys. Chem.* **99**, 16380 (1995).
7. Kucherov, A. V., Gerlok, G. L., Jen, H. W., and Shelef, M., *Catal. Today* **27**, 79 (1996).
8. Márquez-Alvarez, C., Rodríguez-Ramos, I., Guerrero-Ruiz, A., Haller, G. L., and Fernández-García, M., *J. Am. Chem. Soc.* **119**, 2905 (1997).
9. Cowan, A. D., Dumplemann, R., and Cant, N. W., *J. Catal.* **151**, 356 (1995).

10. Trovarelli, A., *Catal. Rev. Sci. Eng.* **38**, 439 (1996).
11. (a) Liu, W., Sarofin, A. F., and Flytzani-Stephanopoulos, M., *Chem. Eng. Sci.* **49**, 4871 (1994); (b) Martínez-Arias, A., Soria, J., Cataluña, R., Conesa, J. C., and Cortés, V., to be publised.
12. Cunningham, J., O'Brien, S., Sanz, J., Rojo, J. M., Soria, J., and Fierro, J. L. G., *J. Mol. Catal.* **57**, 379 (1990).
13. Soria, J., Coronado, J. M., and Conesa, J. C., *J. Chem. Soc. Faraday Trans.* **92**, 1619 (1996).
14. Dow, W. P., Yang, Y. P., and Hwang, T. J., *J. Catal.* **160**, 155 (1996).
15. Bechara, R., Abukais, A., and Bonell, J.-P., *J. Chem. Soc. Faraday Trans.* **89**, 1257 (1993).
16. Kester, E., Gillot, B., Perriat, P., Dufour, Ph., Villete, C., Tailhades, Ph., and Rousset, A., *J. Solid State Chem.* **126**, 7 (1996).
17. "Handbook of X-ray Photo Electron Spectroscopy." Perkin-Elmer, New York, 1978.
18. Grunet, W., Hayes, N. W., Joyner, R. W., Shpiro, E. S., Siddiqui, M. R. H., and Baera, G. N., *J. Phys. Chem.* **42**, 10832 (1992).
19. Carley, A. F., Rajumon, M. K., and Robetrs, M. W., *J. Sol. St. Chem.* **106**, 156 (1993).
20. (a) Shyu, J. Z., Otto, K., Watkings, W. L. H., Graham, G. W., Belitz, R. K., and Ghandi, M. S., *J. Catal.* **114**, 23 (1988); (b) Schmitz, P. J., Usmen, R. K., Peters, C. R., Graham, G. W., and McCabe, R. W., *Appl. Surf. Sci.* **72**, 181 (1993).
21. Tanaka, M., Shishido, T., Horiuchi, H., Toyota, N., Shindo, D., and Fukuda, T., *J. Alloys Comput.* **192**, 87 (1993).
22. Soria, J., Conesa, J. C., Martínez-Arias, A., and Coronado, J. M., *Sol. St. Ionics* **63/65**, 755 (1993).
23. Hall, W. K., and Vaylon, J., *Catal. Lett.* **15**, 311 (1992).
24. Hierl, R., Urbach, H.-P., and Knozinger, H., *J. Chem. Soc. Faraday Trans.* **88**, 355 (1992).
25. Bowker, K. J., "Eight Peak Index of Mass Spectra." Unwin, Surrey, 1983.
26. Hollins, P., *Surf. Sci. Rep.* **16**, 51 (1992).
27. Kohler, M. A., Cant, N. W., Wainwright, M. S., and Trimm, D. L., *J. Catal.* **117**, 188 (1989).
28. Haller, G. L., and Resasco, D. E., *Adav. Catal.* **36**, 173 (1989).
29. Bernal, S., Botana, F. J., Calvino, J. J., Cauqui, M. A., Cifredo, G. A., Jobacho, A., Pintado, J. M., and Rodríguez-Izquierdo, J. M., *J. Phys. Chem.* **97**, 4118 (1993).
30. Balkenende, R., Hoodegan, R., de Beer, T., Gijzeman, O. L., and Geus, J. W., *Appl. Surf. Sci.* **55**, 18 (1992).
31. Cataluña, R., Ph.D. thesis, Universidad Complutense, Spain, 1995.